Received: 11 October 2022 | Revised: 24 December 2022 | Accepted: 13 January 2023

DOI: 10.1002/mrm.29605

Magnetic Resonance in Medicine

TECHNICAL NOTE

Diffusion sampling schemes: A generalized methodology with nongeometric criteria

Justino R. Rodríguez-Galván | **Guillem París** | **Antonio Tristán-Vega** | **Carlos Alberola-López**

Laboratorio de Procesado de Imagen (LPI), Universidad de Valladolid, Valladolid, Spain

Correspondence
Justino R. Rodríguez-Galván, Universidad de Valladolid, ETSI de Telecomunicación, Campus Miguel Delibes, 47011 Valladolid, Spain.
Email: jrodgal@lpi.tel.uva.es

Funding information
Agencia Estatal de Investigación, Grant/Award Numbers: PID2020-115339RB-I00, RTI2018-094569-B-I00, TED2021-130090B-I00; ESAOTE, Ltd., Grant/Award Number: 18IQBM

Purpose: The aim of this paper is to show that geometrical criteria for designing multishell q-space sampling procedures do not necessarily translate into reconstruction matrices with high figures of merit commonly used in the compressed sensing theory. In addition, we show that a well-known method for visiting k-space in radial three-dimensional acquisitions, namely, the Spiral Phyllotaxis, is a competitive initialization for the optimization of our nonconvex objective function.

Theory and Methods: We propose the gradient design method WISH (WeIghting SHells) which uses an objective function that accounts for weighted distances between gradients within M-tuples of consecutive shells, with M ranging between 1 and the maximum number of shells S. All the M-tuples share the same weight ω_M. The objective function is optimized for a sample of these weights, using Spiral Phyllotaxis as initialization. State-of-the-art General Electrostatic Energy Minimization (GEEM) and Spherical Codes (SC) were used for comparison. For the three methods, reconstruction matrices of the attenuation signal using MAP-MRI were tested using figures of merit borrowed from the Compressed Sensing theory (namely, Restricted Isometry Property —RIP— and Coherence); we also tested the gradient design using a geometric criterion based on Voronoi cells.

Results: For RIP and Coherence, WISH got better results in at least one combination of weights, whilst the criterion based on Voronoi cells showed an unrelated pattern.

Conclusion: The versatility provided by WISH is supported by better results. Optimization in the weight parameter space is likely to provide additional improvements. For a practical design with an intermediate number of gradients, our results recommend to carry out the methodology here used to determine the appropriate gradient table.

KEYWORDS
coherence, diffusion MRI, q-space sampling, Voronoi

1 | INTRODUCTION

Within the last decades, the trends in Diffusion MRI (dMRI) have moved from the Gaussian assumption underneath Diffusion Tensor Imaging toward sophisticated biological models or sparse signal representations. The field has evolved in parallel with the widespread adoption of advanced acquisition protocols for Diffusion Weighted Images, comprising several tens to hundreds of gradient diffusion directions with variable strengths (the so-called b-value, measured in [s/mm^2]) so that the "q-space" is covered. Actually, as maximum reachable b-values have increased, non-Gaussian diffusion patterns have been evidenced and hence the need of more involved models has arisen. Although several arrangements are possible (Cartesian, randomized, etc.), multishell samplings have become the de facto standard: with this approach, the samples are distributed among a pre-defined set of so-called shells, that is, spheres with a fixed b-value. At each shell, a predefined number of gradient directions are evenly spaced covering (half the) orientations space.

To completely describe the sampling, however, it is necessary to determine how different shells are interleaved, that is, whether the samples in one shell should fill the gaps between those in other shells or they should replicate the same locations, see Figure 1. Several popular approaches advocate for the former: both the General Electrostatic Energy Minimization (GEEM)[1] and the Spherical Codes (SC)[2] pursue schemes where not only the directions at each shell, but also the whole set of gradients when they are collapsed in a single sphere, remain evenly spaced. This design, sketched in Figure 1A, is optimal under the point of view of orientations space coverage, and it is typically sought by optimizing a cost function that accounts for both the within-shell and the "collapsed" gradient distances.

However, it is not clear if a geometrically optimal sampling will be equally optimal with regard to the numerical behavior of reconstruction problems within dMRI. For example, the interleaving model sketched in Figure 1B might be a reasonable choice, but it is banned by construction with the aforementioned approaches.[1,2]

Here, we propose a more flexible design by systematically defining weighted cost functions for each possible combination of M consecutive shells. This way, we can pursue the design in Figure 1A by penalizing the onefold and the threefold combinations of shells; or we can pursue Figure 1B by penalizing onefold and twofold combinations; or we can pursue any intermediate solution by properly weighting all one-, two-, and threefold combinations. In order to test the potential benefit of this approach, we define performance figures not grounded on geometrical considerations, but instead on the properties of resulting reconstruction matrices. They serve to draw counterexamples demonstrating that raw geometrical constraints might be suboptimal for the design of multishell sampling schemes.

Finally, we notice that the definition of a rather complex cost function to optimize turns the problem heavily nonconvex. To cope with convergence issues, we propose the use of Spiral Phyllotaxis[3] as a suitable and efficient initialization for Newton–Raphson's iterations. Up to our knowledge, this is also a novel contribution of our work. In practical terms, our methodology lets us find an appropriate weighting for the one-, two-, and threefold combinations referred to above that optimizes a figure of merit related to the quality of the reconstruction matrix. This search is facilitated by the initialization just mentioned, as opposed to a random initialization since, on average, the former overcomes the latter. This will also be quantified.

2 | THEORY

2.1 | State-of-the-art q-space methods

We have categorized q-space sampling scheme methods in three stages:

a. First attempts were characterized by the use of regular polyhedra and Archimedes' solidus vertices to locate gradients, taking advantage of their natural distribution.[4] This method was refined by interlacing of polyhedra on different layers for multishell approaches.[5]

b. An alternative approached stemmed from considering gradients as electrons, and optimizing their distribution by EEM.[6] One of these methods was selected for the Human Connectome Project (HCP).[7] This method, referred to as General EEM (GEEM),[1] pursues to minimize this energy by defining a two-term cost function

$$V = \alpha V_1 + (1-\alpha)V_2, \tag{1}$$

where V_1 models the energy of the gradient distribution over one shell and V_2 the energy of the interaction between every two shells. Specifically:

$$V_1 = \frac{1}{S}\sum_{s=1}^{S}\frac{1}{K_s^2}\sum_{i<j} v(\mathbf{u}_{s,i}, \mathbf{u}_{s,j}), \tag{1a}$$

$$V_2 = \frac{1}{K^2}\sum_{\substack{s,t \\ s\neq t}}\sum_{i=1}^{K_s}\sum_{j=1}^{K_t} v(\mathbf{u}_{s,i}, \mathbf{u}_{t,j}), \tag{1b}$$

with S the number of shells, K the number of gradients, K_i, with $i \in \{s,t\}$ the number of gradients in

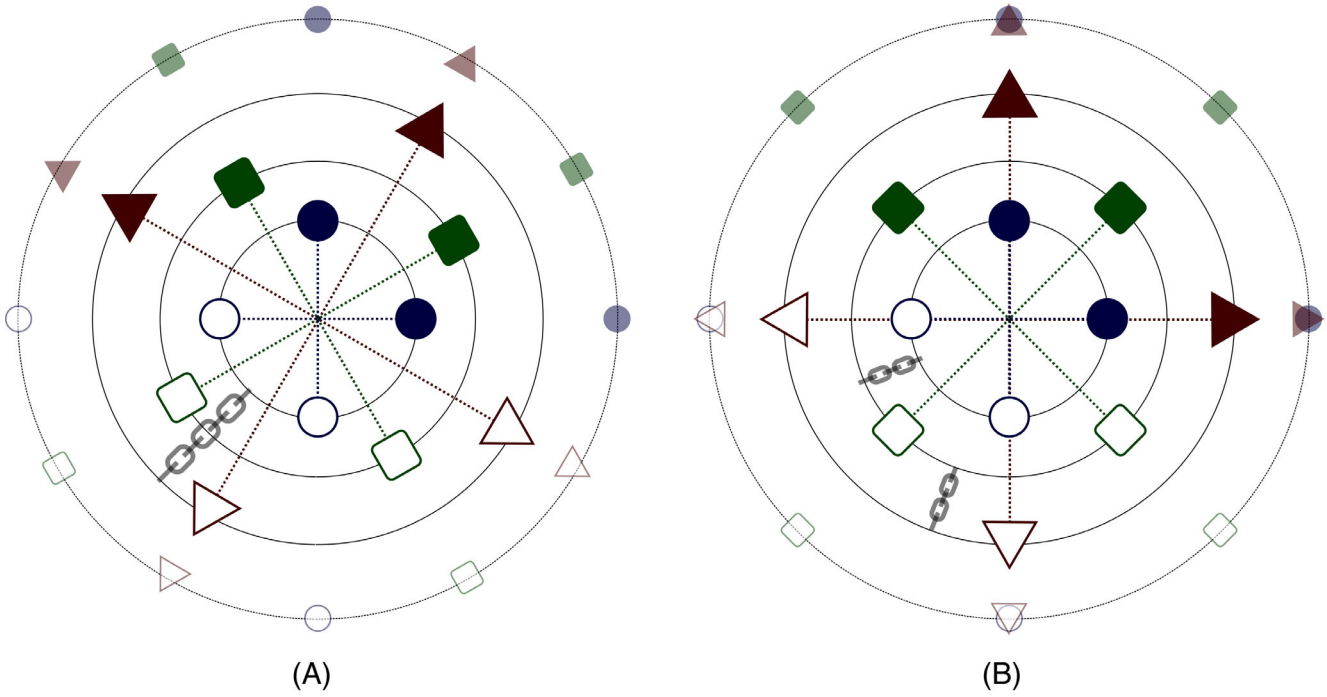

FIGURE 1 A two-dimensional sketch of two possible designs for 3 shells (solid-line circumferences) with two gradient directions each (filled forms). The symmetric antipodes are also represented (empty forms). The outermost, dashed circumference represents the overall distribution of sampled directions with all shells collapsed. In both cases, the samples at each shell are expected to be evenly spaced, however: (A) the three shells are linked altogether in the cost function pursuing an overall even distribution in the collapsed shell; (B) only twofold subsets are linked together, so that consecutive shells are better interleaved at the expense of a worse overall distribution.

shell i, $K = \sum_{i=1}^{S} K_i$, and $\mathbf{u}_{t,j}$ the jth gradient in shell t. Throughout this note, gradients are considered as directions, that is, their moduli equal 1, regardless of the shell they belong to. Function $v(\mathbf{u}, \mathbf{v})$ defined the electrostatic repulsion force

$$v(\mathbf{u}, \mathbf{v}) = \frac{1}{\|\mathbf{u} - \mathbf{v}\|^2} + \frac{1}{\|\mathbf{u} + \mathbf{v}\|^2}. \tag{2}$$

Notice that in Equation (1a) shells are inversely weighted by K_s^2 so that no shell is privileged.

c. A more recent alternative uses SC to locate gradients in multishell problems. It is based on the concept of *covering radius*, which applies both to one and to all the samples in the same shell, and are respectively defined as:

$$d_i(\{\mathbf{u}_l\}_{l=1}^{K}) = \min_{j \neq i,\ \forall j} \arccos |\mathbf{u}_i^T \mathbf{u}_j|, \tag{3a}$$

$$d(\{\mathbf{u}_l\}_{l=1}^{K}) = \min_i d_i(\{\mathbf{u}_l\}_{l=1}^{K}) = \min_{j \neq i,\ \forall i,\ \forall j} \arccos |\mathbf{u}_i^T \mathbf{u}_j|, \tag{3b}$$

with $\{\mathbf{u}_i \in \mathbb{S}^2\}_{i=1}^{K}$ and $\mathbb{S}^2$ stands for a continuous sphere of some radius. For the monoshell problem, the function to optimize is Equation (3b). For the multishell case, the target function is

$$\max_{\{\mathbf{u}_{s,i} \in \mathbb{D}\}} \omega S^{-1} \sum_{s=1}^{S} d\left(\{\mathbf{u}_{s,i}\}_{i=1}^{K_s}\right) + (1-\omega) d(\{\mathbf{u}_{s,i}\}_{i=1,\ldots,K_s; s=1,\ldots,S}), \tag{4}$$

with $\mathbb{D} \subseteq \mathbb{S}^2$ the solution domain. In our case of interest —referred to in Reference 2 as the continuous problem— $\mathbb{D} = \mathbb{S}^2$. Notice that Equation (4) contains interactions (i.e., the covering radius) of gradients within the same shell as well as interaction between pairs of gradients from every two shells.

As previously described in (b) and (c), both methods have weighting parameters α and ω, respectively, in Equations (1) and (4), which are hardwired to the value 0.5.

2.2 | Reconstruction matrix

A central problem to dMRI is that of fitting the diffusion profile $E(\mathbf{q})$ as the superposition of a set of N basis functions up from K measurements within the q-space.

This can be cast into a linear problem:

$$\mathbf{E} \simeq \mathbf{A}\,\mathbf{c} \;\Rightarrow\; \mathbf{c}^* = \arg\min_{\mathbf{c}} \|\mathbf{E} - \mathbf{A}\,\mathbf{c}\|^2 + \lambda\, P(\mathbf{c}), \quad (5)$$

where the $K \times 1$ vector $\mathbf{E}$ stacks the q-space measurements: $[\mathbf{E}]_k = E(\mathbf{q}_k) = E(q_k\mathbf{u}_k), k = 1, \ldots, K$; q_k is related to the kth b-value through the effective diffusion time τ as $b_k = 4\pi^2\tau q_k^2$; the rightmost addend, weighted by the positive constant λ, is a penalty defined by a function $P(\cdot)$ that prevents *irregular* solutions; $\mathbf{A}$ is the $K \times N$ reconstruction matrix, so that $[\mathbf{A}]_{k,n} = \Phi_n(\mathbf{q}_k)$ for some functional basis $\{\Phi_n(\cdot)\}_{n=1}^N$ and $\mathbf{c}$ is the coefficient vector that locally adapts the signal model to the observed diffusion pattern. Owing to its widespread use by the dMRI community, we will consider here the Mean Apparent Propagator approach.[8] In brief: let $\mathbf{D}$ be the diffusion tensor computed at each voxel, and let $\mathbf{B}' = 2\tau\mathbf{D} = \mathbf{R}\,\mathbf{B}\,\mathbf{R}^T$ be the eigen-decomposition of $\mathbf{B}'$, with $\mathbf{R}$ orthonormal so that $[q_x, q_y, q_z] = \mathbf{R}^T\mathbf{q}$ rotates the q-vector to the *anatomical frame*, and $\mathbf{B} = \mathrm{diag}([\beta_x, \beta_y, \beta_z])$. Then:

$$\Phi_{n_1,n_2,n_3}(\mathbf{q};\mathbf{D}) = \phi_{n_1}(\beta_x, q_x)\cdot\phi_{n_2}(\beta_y, q_y)\cdot\phi_{n_3}(\beta_z, q_z);$$
$$\text{with}\;\; \phi_n(\beta, q) = \frac{i^{-n}}{\sqrt{2^n n!}} e^{-2\pi^2 q^2\beta^2} H_n(2\pi\beta q), \quad (6)$$

where $H_n(\cdot)$ stands for the nth Hermite polynomial. The three indices $\{n_1, n_2, n_3\}$ fulfill $n_1 + n_2 + n_3 = L$ for each L from 0 to a predefined maximum order $L_{\max}$, so that $N = (L_{\max} + 1)(L_{\max} + 2)/2$.

2.3 | Figures of merit

The method described in Section 2.2 provides reconstruction matrices, the quality of which in terms of reconstruction capabilities can be measured by borrowing figures from the Compressive (or Compressed) Sensing theory,[9] specifically, *Coherence* and *Restricted Isometry Property* (see Reference 10 for a high-level description of these metrics and section 1.3 of Reference 9 for a deeper and math-oriented insight).

We depart from matrix $\mathbf{A} \in \mathbb{C}^{m\times L}$. Let P denote the set of indices $P = \{1, \ldots, L\}$ and let $Q \subset P$. In addition, we define $\|\mathbf{x}\|_p, x \in \mathbb{C}^m = \left(\sum_{i=1}^m |x_i|^p\right)^{\frac{1}{p}}$. This operation will be referred to as p-norm of vector $\mathbf{x}$, or ℓ_p for short. For matrices, $\|\mathbf{A}\|_{2\to 2} = \sigma_{\max}(\mathbf{A})$, with $\sigma_{\max}(\mathbf{A})$ the maximum singular value of matrix $\mathbf{A}$. In addition, let $\mathbf{A}_Q$ denote the submatrix of $\mathbf{A}$ with columns indexed by Q.

2.3.1 | Coherence

Let matrix $\mathbf{A}$ have ℓ_2 normalized columns, that is, $\|\mathbf{a}_i\|_2 = 1$, $1 \le i \le L$. Then the ℓ_1 coherence function $\mu_1(s)$ of this matrix is defined as

$$\mu_1(s) := \max_{i\in P} \max \left\{ \sum_{j\in Q} |\mathbf{a}_i^T\mathbf{a}_j|, Q \in P, \mathrm{Card}(Q) = s, i \notin Q \right\}. \quad (7)$$

This function generalizes the *coherence* of matrix $\mathbf{A}$, defined as $\mu = \max_{1\le i\ne j\le N} \left|\mathbf{a}_i^T\mathbf{a}_j\right|$, since $\mu = \mu_1(s = 1)$. Generally speaking, the lower the coherence, the better behaved the reconstruction problem.

2.3.2 | Restricted isometry property

The sth restricted isometry constant $\delta(s)$ is defined as

$$\delta(s) := \max_{Q\subset P, \mathrm{Card}(Q)\le s} \left\|\mathbf{A}_Q^H\mathbf{A}_Q - \mathbf{I}\right\|_{2\to 2}, \quad (8)$$

with $1 \le s \le L - 1$. In this case, no ℓ_2 normalized columns are mandatory. Once again, the smaller the Restricted Isometry Property (RIP), the better behaved the reconstruction problem.

2.3.3 | Voronoi cells

The Voronoi cell[11] of a site is defined as the polygonal region which encloses the nearest points to that site. Regions boundaries are made by equidistant points of the closest sites. The related figure of merit to this measurement is the distribution of the areas of each region. In geometrical terms, better gradient distribution would be those that give rise to Voronoi cells with large areas as well as small variability in their values. Notice that this third measure does not make use of reconstruction matrix $\mathbf{A}$ and it is a purely geometric measure.

3 | METHODS

3.1 | Cost function

Let $G = \{\mathbf{g}_i\}_{i=1}^K$ be an arbitrary set of K gradient directions. We first define the average distance associated to G as:

$$Q(G) = \sum_{i=1}^K \sum_{j=i+1}^K \frac{1}{\sin(\angle\mathbf{u}_i, \mathbf{u}_j)},$$
$$\text{for:}\;\; \sin(\angle\mathbf{u}_i, \mathbf{u}_j) = \sqrt{1 - (\mathbf{u}_i^T\mathbf{u}_j)^2}, \quad (9)$$

so that the smaller $Q(G)$ the more evenly spaced the gradients in G become. This function uses, in essence, the same

trigonometric information as SC uses, and allows us to deal with antipodal gradients by means of a single expression, while GEEM requires the two terms in Equation (2). Next, let $\{G_s\}_{s=1}^{S}$ be the S shells to design, with numbers of gradients $\mathrm{Card}(G_s) = K_s$ each. After Figure 1, we pursue even distributions of M-fold combinations of consecutive shells, with $M = 1, 2, \ldots, S$. Hence, for each M, we define:

$$\mathcal{G}_m^M = \bigcup_{s=m}^{m+M-1} G_s, \text{ for: } m = 1, \ldots, S - M + 1. \quad (10)$$

In Figure 1A, only $M = 1$ (each shell individually) and $M = 3$ (all shells together) are used. On the contrary, in Figure 1B $M = 1$ and $M = 2$ are used, that is, individual shells plus the two interactions between shells 1 and 2 and 2 and 3. This way, we can explicitly drop down the interaction between shells 1 and 3 to attain a different interleaving. This rationale can be generalized by setting up a cost function where each M-fold combination can be weighted at will:

$$\mathcal{Q} = \sum_{M=1}^{S} \omega_M \underbrace{\sum_{m=1}^{S-M+1} \frac{1}{\rho\left(K_m^M\right)} Q\left(\mathcal{G}_m^M\right)}_{q_M} = \sum_{M=1}^{S} \omega_M \, q_M, \quad (11)$$

where $K_m^M = \mathrm{Card}(\mathcal{G}_m^M)$ and $\rho(K) = Q\left(G_{\mathrm{opt},K}\right)$ for a set $G_{\mathrm{opt},K}$ of K gradients optimized in isolation, that is, $\rho\left(K_m^M\right)$ is the minimum attainable value of $Q\left(\mathcal{G}_m^M\right)$. The weights $\{\omega_M\}_{M=1}^{S}$ are the design parameters that endow our method with an improved flexibility.

3.2 | Initialization

Initialization to optimize Equation (11) is made by the Spiral Phyllotaxis:[3] let $1 \le k_s \le K_s$ index the gradients within the sth shell; let $1 \le k \le K$, $K = \sum_{s=1}^{S} K_s$, index the whole set of gradients obtained by placing all S shells in a row; let $\psi[s, k_s] = \sum_{t=1}^{s-1} K_t + k_s$ be the function that maps the k_sth gradient of the sth shell to its global index k. Then:

$$\varphi_k = k \cdot \varphi_{\mathrm{gold}}, \text{ with: } \varphi_{\mathrm{gold}} = \pi(3 - \sqrt{5}); \quad (12)$$

$$\theta_k \equiv \theta_{\psi[s,k_s]} = \alpha_{k_s}, \text{ with: } \alpha_{k_s} = \frac{\pi}{2} \cdot \sqrt{\frac{k_s}{K_s}}, \quad (13)$$

are the elevation and azimuth of the kth gradient direction. Our method, based on the minimization of Equation (11) with regular Newton–Raphson's iterations from the previous initialization, will be hereafter referred to as WISH (WeIghting SHells).

3.3 | Experimentation

The first experiment is intended to check the consistency of the cost function postulated in Section 3.1. The benchmark will be the design of three shells with 90 gradient directions each. The three (unweighted) addends $\{q_M\}_{M=1}^{3}$ of the outermost sum in Equation (11) are then evaluated after $\mathcal{Q}(G)$ has been optimized, and this procedure is repeated for all possible combinations of the three weights $\{\omega_M\}_{M=1}^{3}$. Note that multiplying these weights by a constant will just lead to a scaled version of the cost function, so that without any loss of generality we can probe only those combinations fulfilling $\omega_1 + \omega_2 + \omega_3 = 1$. Accordingly, for each probed value of ω_1, we will sweep $\omega_2 \in [0, 1 - \omega_1]$ and fix $\omega_3 = 1 - \omega_1 - \omega_2$.

The second experiment is a comparison of the three optimization schemes (namely, GEEM, SC, and WISH). We have tested the four combinations of coefficients w_M, $1 \le M \le 3$, indicated in Figure 3(i). Then for each combination and optimization procedure we have calculated both Coherence and RIP—following Equations (7) and (8)— for three values of parameter s, namely $s = \{1, 2, 3\}$, of the MAP reconstruction matrices that result from each method. In order to test the benefits of the initial solution proposed in Section 3.2, the optimization of function in Equation (11) has also been initialized with 500 random realizations of the gradients, uniformly distributed in the three spheres. Finally, for this second experiment, we also calculate the distribution of Voronoi cell areas, to gain insight into a geometrical interpretation.

The third experiment is intended to test the impact of the multishell designs in actual reconstruction problems. To this end, we have borrowed the methodology in Reference 12; specifically, departing from a statistical characterization of the biological properties of relevant structures within the white matter, the NODDI approach[13] is used to generate random models of one-, two-, or three-crossing fibers that mimic a wide variety of white matter voxels. These models are used to simulate the signal acquired with either multi-shell scheme designed (at a peak signal-to-noise ratio [SNR] of 16 or 32) and as ground-truth that the MAPL-reconstructed (Laplacian regularized MAP-MRI) signals are compared to through the relative mean squared error.

4 | RESULTS

Figure 2 shows the results of the first experiment; in the five plots, we show the value of the terms $\{q_M\}_{M=1}^{3}$, respectively, in colors red, green, and blue. The variable in the horizontal axis is ω_2 and plots (a) through (e) are parameterized by ω_1, for values $\{0, 1/3, 1/4, 1/3, 1/2\}$.

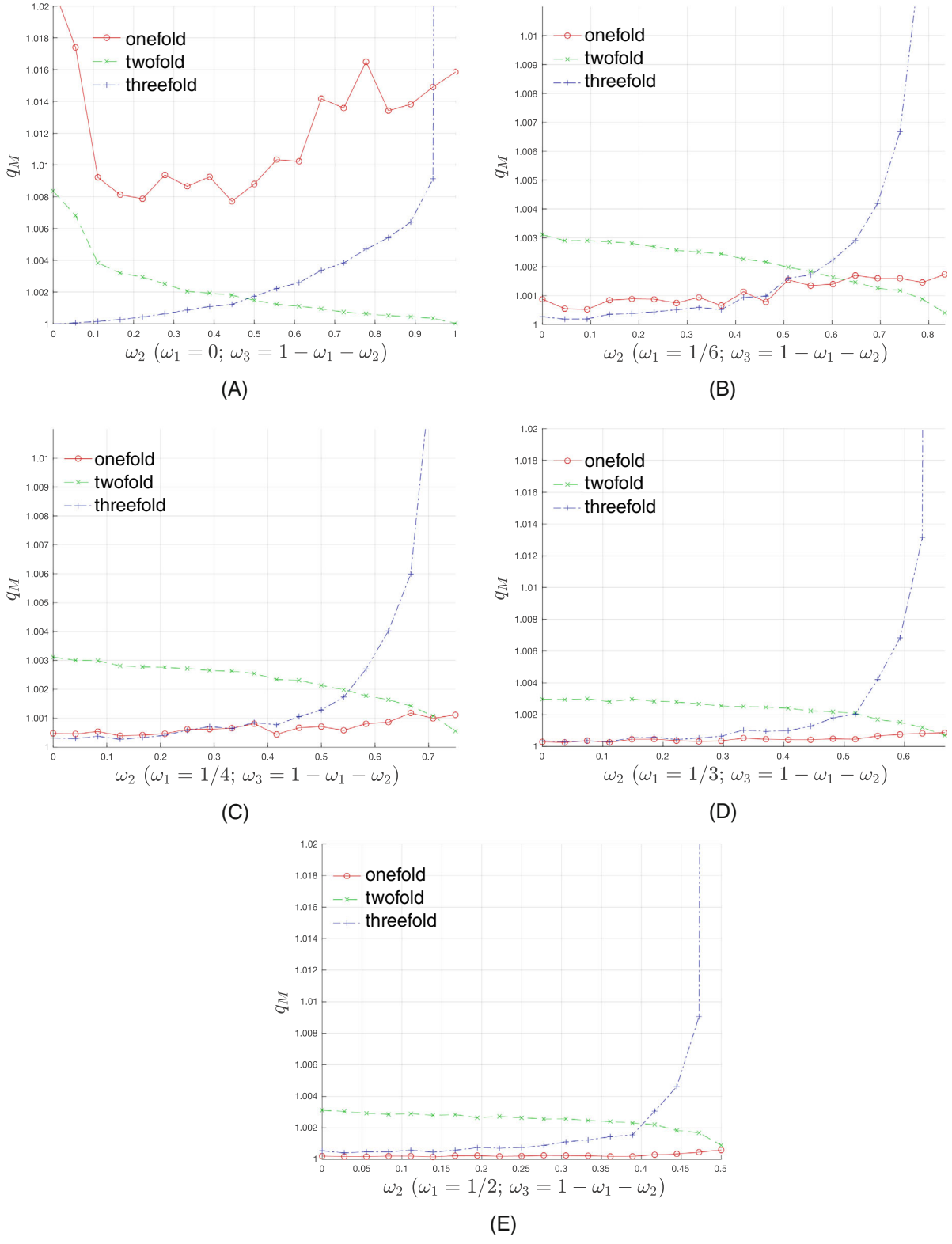

FIGURE 2 Experiment 1: Values of q^M in Equation (11) as a function of ω_2 parameterized by ω_1: q^1 red, q^2 green, q^3 blue

Figure 3(ii) shows the result of the second experiment; in this case, plots labeled with (a) and (b) represent Coherence and those with (c) and (d) RIP for either 3×30 gradients (leftmost figures) and 3×90 (rightmost). *Combination* stands for each row in Table 3(i).For each combination, the values actually represented are the difference between the result of the methods used for comparison (SC, GEEM and random initializations) and WISH;

Index	$(\omega_1, \omega_2, \omega_3)$
1	(1/2, 1/2, 0)
2	(1/2, 1/6, 1/3)
3	(1/6, 1/2, 1/3)
4	(1/2, 0, 1/2)

(i)

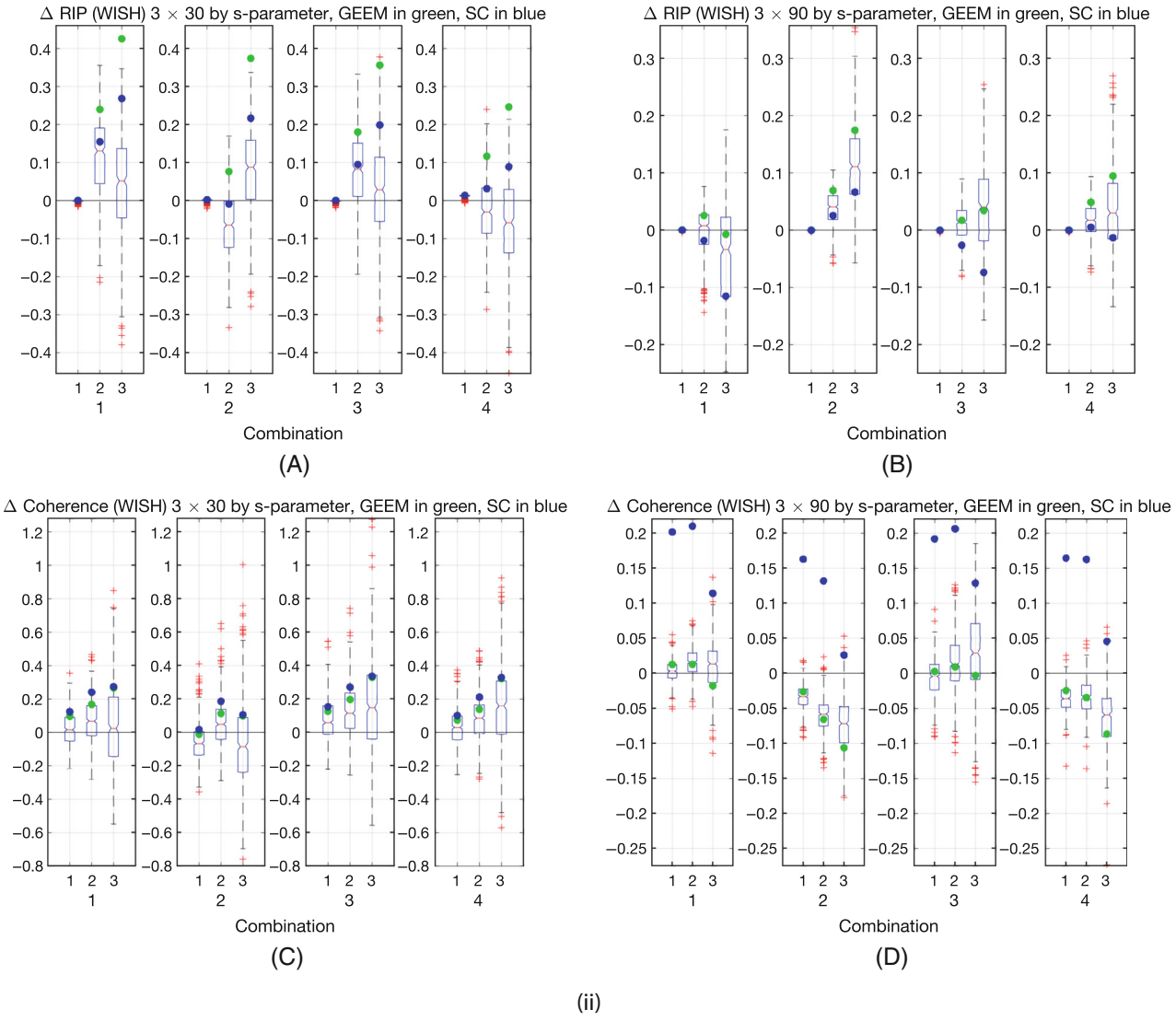

(ii)

FIGURE 3 (i) Table of selected combinations for Experiments 2 and 3. (ii) Experiment 2: Difference of Coherence and Restricted Isometry Property of the reconstruction matrices from Spherical Codes (SC), General Electrostatic Energy Minimization (GEEM) and random initialization with respect to WeIghting SHells (WISH). SC and GEEM are represented by filled circles with colors blue and green respectively. Results from random initializations are shown as boxplots. Level zero has been highlighted for easier reference (positive values favor our method). (a) Coherence for 3 × 30; (b) Coherence for 9 × 30; (c) Restricted Isometry Property for 3 × 30; (d) RIP for 9 × 30.

for to SC and GEEM we have used filled circles with colors green and blue, respectively, while for the random initializations we have used boxplots. The variable in the horizontal axis is parameter *s*. Positive values support our method.

As for Figure 3, we represent the distribution of Voronoi cells areas along the three shells after optimization of gradient directions according to methods WISH, GEEM, and SC. For WISH, the four combinations of parameters in Table 3(i) have been tested, labeled in the

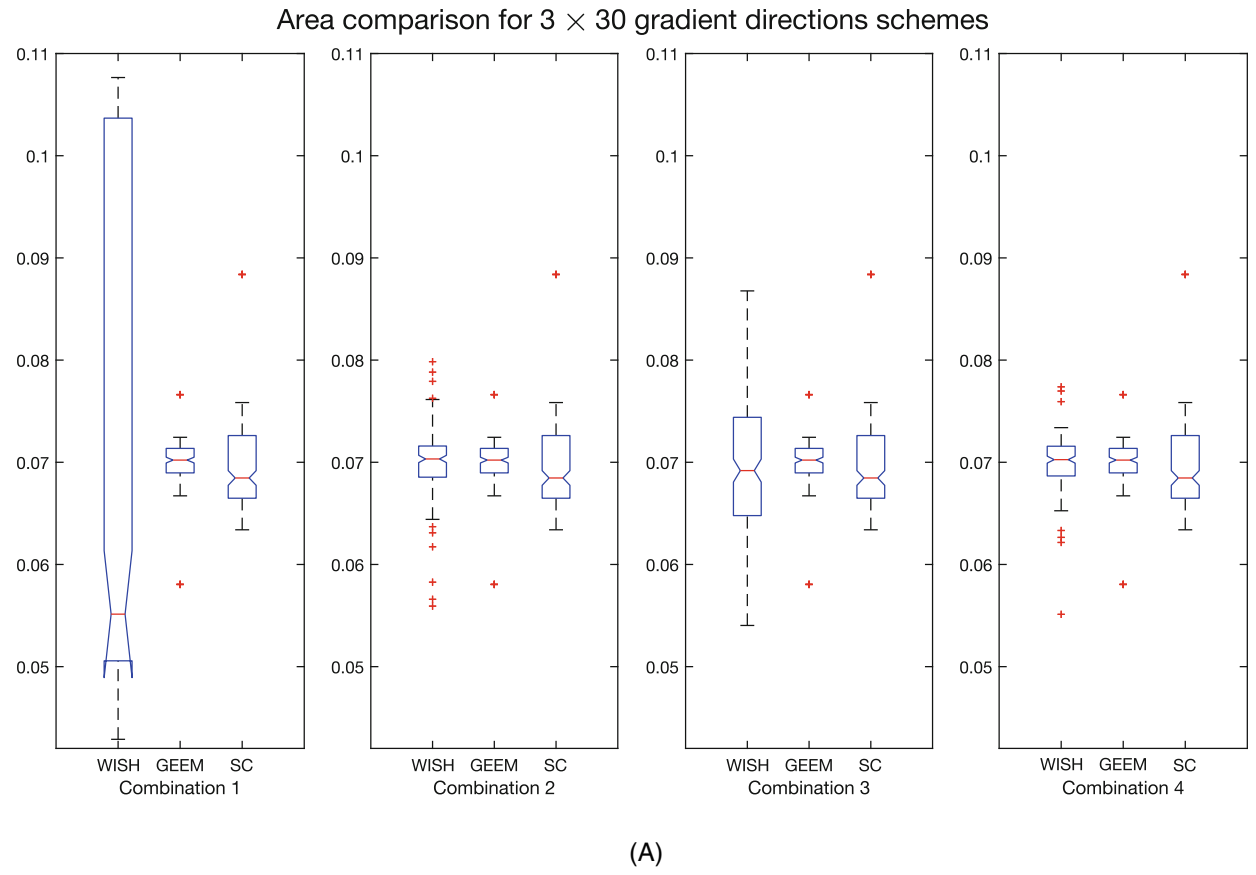

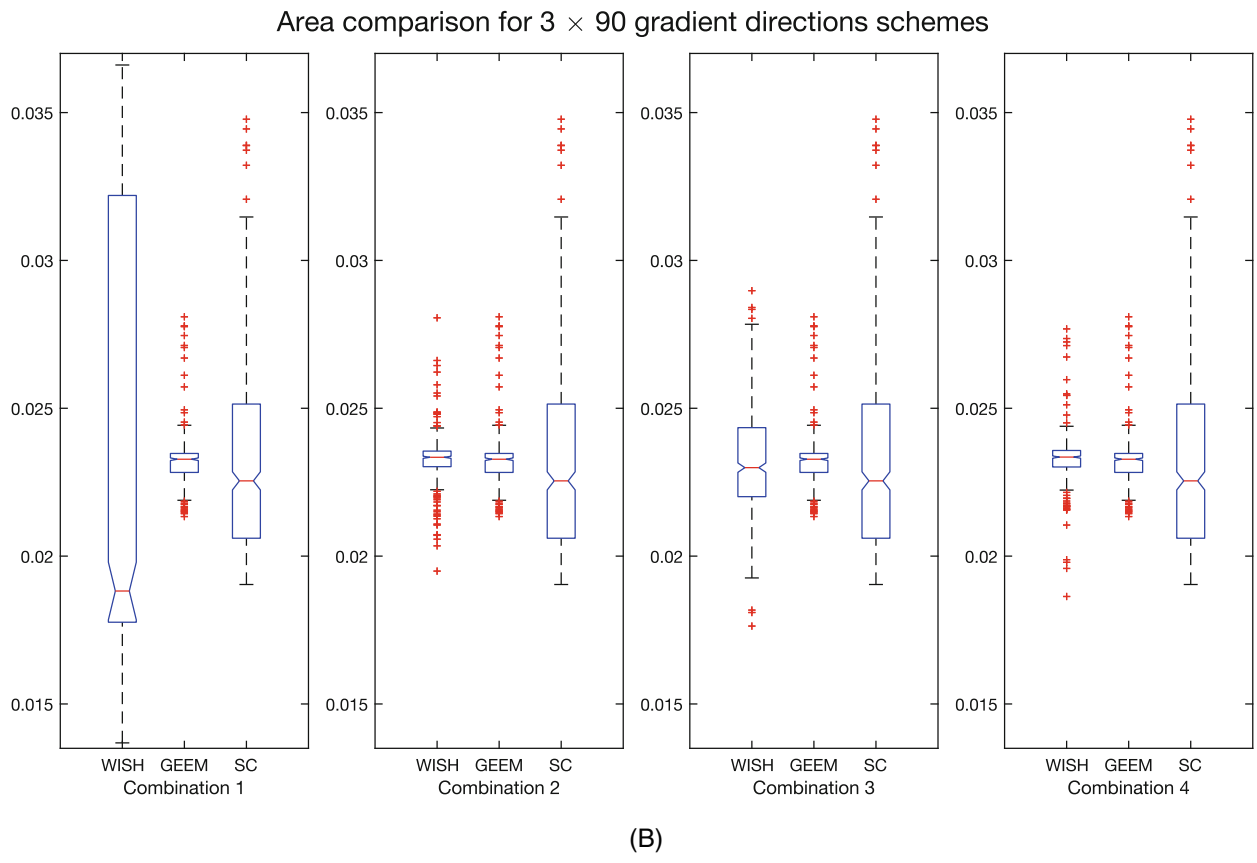

FIGURE 4 Experiment 2: boxplots of the area of Voronoi cells for the four combinations of parameters in Figure 3 (i) and the methods WeIghting SHells, general electrostatic energy minimization, and spherical codes. (A) Experiment 3 × 30; (B) Experiment 3 × 90

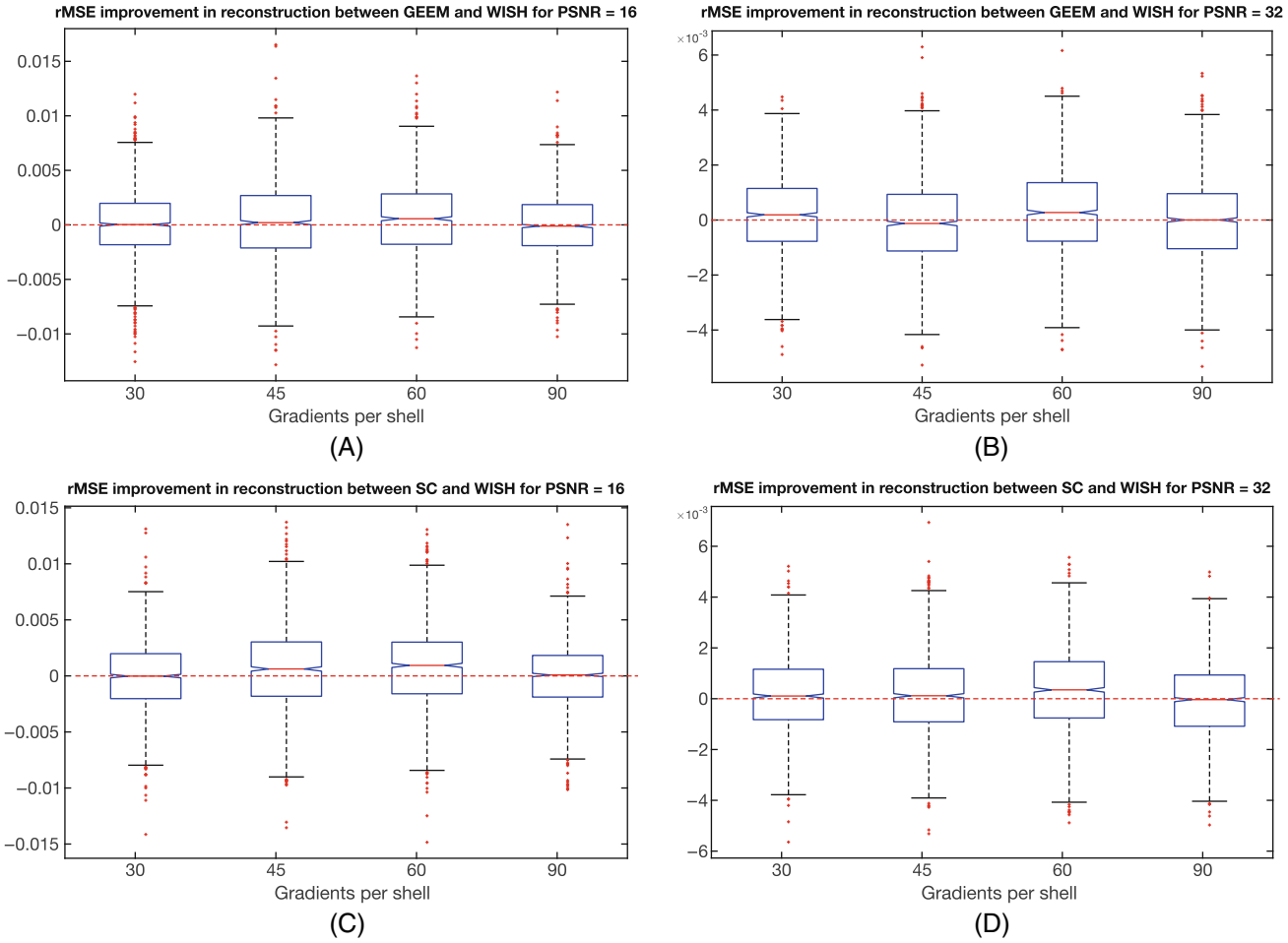

FIGURE 5 Difference of relative mean squared errors on the reconstruction of synthetic data for best restricted isometry property WeIghting SHells (WISH) combination. (A) Between general electrostatic energy minimization (GEEM) and WISH peak signal-to-noise ratio (SNR) 16, (B) between GEEM and WISH peak SNR 32, (C) between spherical codes (SC) and WISH peak SNR 16, (D) between SC and WISH peak SNR 32

figure as Combination 1 through 4. Results are shown for both the experiment 3×30 and experiment 3×90.

The third experiment is shown in Figure 5, where we depict the relative mean squared error improvement of our method with respect to both GEEM (top) or SC (bottom) for peak SNR 16 (left) or 32 (right). We have designed three shells in all cases with a varying number of gradients per shell; as can be seen, our method slightly outperforms the others in many situations and, when improvement is not observed, its performance is virtually identical. As it could be expected, all methods tend to converge when the number of gradients per shell is sufficiently large (90).

5 | DISCUSSION AND CONCLUSIONS

Figure 2 shows that parameters w_M do play a role since the terms q_M defined in Equation (11) reveal a dependence with these parameters. Specifically, the green line in the plots shows a decreasing trend with parameter w_2, while the blue line shows a complementary trend. As for the red line, subfigure (2) shows an erratic behavior for $\omega_1 = 0$, since q_1 is irrelevant for this value, but the decreasing trend is appraised as w_1 increases. Interestingly, this trend is not observed when nonconsecutive shells are allowed to interact in Equation (11) for $M = 2$, since in this case the role of q_2 is essentially taken over by q_3.

The role played by the parameters is highlighted in Figure 3(ii), where we appraise that for 3×30 (leftmost subfigures) we can find a parameter setting (say, *Combinations* 1 or 3) where WISH shows better figures than both GEEM and SC, and the medians of the boxplots of random initializations show a positive bias. Actually, if Gaussianity is accepted for the distributions of random initializations, the probability of requiring at least five random initializations to obtain a better figure than WISH is about 0.40 for $s = 2$ and *Combination* 3, for both Coherence and RIP.

Similar comments apply for the 3×90 case, although different parameters combinations in this case are needed for Coherence (*Combination* 3) and RIP (*Combination* 2); as for random initializations, the same probability as before is now 0.22 for the former and $s = 3$ whereas it reaches 0.79 for the latter and $s = 3$. These results, however, do not have a clear geometric counterpart, as shown in Figure 4, since combinations 1 and 3 for the experiment 3×30 do not seem to favor WISH with respect to GEEM and SC, either in terms of higher median or lower variance (subfigure (A)). This seems to be also the case for the 3×90 case (subfigure (B)) in which albeit combination 2 seems favorable to our method, combination 3 does not. Hence geometric criteria may not be the only ones to consider for the design of diffusion sampling schemes as our counterexample reveals. Concerning Figure 5, and as it might be expected beforehand—due to the subtle improvement of SC over GEEM reported in Reference 2—differences are not dramatic, but we attain a consistent improvement for the mid-range of gradient directions per shell: for 45 and 60 gradient directions, the notches in the box plots indicate that our method's median values outperform the other methods within a confidence interval (except for GEEM with the—otherwise very high—peak SNR value of 32).

Hence, these results support that M-fold combinations of consecutive shells, $M = 1, 2 \ldots, S$, provide degrees of flexibility to optimize the figure of merit of choice, and optimizing these figures is not necessarily accompanied by an obvious geometric signature. In addition, this methodology carries over to other methods not based on the linear model in Equation (5) as long as a proper figure of merit is defined and optimized in the weighting parameter space. Consequently, and as further research, rather than sampling a small set of values in the $\{\omega_1, \omega_2, \omega_3\}$ space, as carried out in the paper, these parameters could be target variables of an outer optimization loop to maximize the reconstruction matrix quality for the linear case, or some figure of merit—to be designed—for a more general case.

ACKNOWLEDGMENTS

This work was supported in part by the Agencia Estatal de Investigación, under Grants RTI2018-094569-B-I00, PID2020-115339RB-I00 and TED2021-130090B-I00 and by the company ESAOTE Ltd by grant 18IQBM.

FUNDING INFORMATION

This work was supported in part by the Agencia Estatal de Investigación, under Grants RTI2018-094569-B-I00, PID2020-115339RB-I00 and TED2021-130090B-I00 and by the company ESAOTE Ltd by grant 18IQBM.

CONFLICT OF INTEREST

The authors declare there is no conflict of interest.

DATA AVAILABILITY STATEMENT

For each method we have used the provided software by the authors:

1. GEEM is written in Python. Accessible through GitHub's package `qspace`[1] at https://github.com/ecaruyer/qspace.
2. SC is written both in C++ and MATLAB. It is also accessible through GitHub's package `dmritool`[2] at https://github.com/DiffusionMRITool/dmritool.
3. WISH code is written entirely on MATLAB. It is accessible through the package `dmrimatlab` at https://www.lpi.tel.uva.es/dmrilab.

ORCID

Justino R. Rodríguez-Galván https://orcid.org/0000-0003-2390-5390
Guillem París https://orcid.org/0000-0002-1564-1199
Antonio Tristán-Vega https://orcid.org/0000-0002-4614-2501
Carlos Alberola-López https://orcid.org/0000-0003-3684-0055

REFERENCES

1. Caruyer E, Lenglet C, Sapiro G, Deriche R. Design of multishell sampling schemes with uniform coverage in diffusion MRI. *Magn Resonan Med*. 2013;69:1534-1540.
2. Cheng J, Shen D, Yap PT, Basser PJ. Single-and multiple-shell uniform sampling schemes for diffusion MRI using spherical codes. *IEEE Trans Med Imag*. 2017;37:185-199.
3. Piccini D, Littmann A, Nielles-Vallespin S, Zenge MO. Spiral phyllotaxis: the natural way to construct a 3D radial trajectory in MRI. *Magn Resonan Med*. 2011;66:1049-1056.
4. Muthupallai R, Holder C, Song A, Dixon W. Navigator aided, multishot EPI diffusion images of brain with complete orientation and anisotropy information. Paper presented at: Proceedings of the 7th Annual Meeting of ISMRM; 1999; Philadelphia, PA: 1825.
5. Ye W, Portnoy S, Entezari A, Blackband SJ, Vemuri BC. An efficient interlaced multi-shell sampling scheme for reconstruction of diffusion propagators. *IEEE Trans Med Imag*. 2012;31:1043-1050.
6. Jones DK, Horsfield MA, Simmons A. Optimal strategies for measuring diffusion in anisotropic systems by magnetic resonance imaging. *Magn Resonan Med*. 1999;42:515-525.
7. Van Essen DC, Ugurbil K, Auerbach E, et al. The human Connectome Project: a data acquisition perspective. *Neuroimage*. 2012;62:2222-2231.
8. Özarslan E, Koay CG, Shepherd TM, et al. Mean apparent propagator (MAP) MRI: a novel diffusion imaging method for mapping tissue microstructure. *NeuroImage*. 2013;78:16-32.
9. Foucart S, Rauhut H. *A Mathematical Introduction to Compressive Sensing*. Birkhauser; 2013.

10. Baraniuk RG. Compressive sensing [lecture notes]. *IEEE Signal Process Mag*. 2007;24:118-121.
11. Aurenhammer F. Voronoi diagrams—a survey of a fundamental geometric data structure. *ACM Comput Surv*. 1991;23:345-405.
12. Tristán-Vega A, Aja-Fernández S. Efficient and accurate EAP imaging from multi-shell dMRI with micro-structure adaptive convolution kernels and dual Fourier Integral Transforms (MiS-FIT). *NeuroImage*. 2021;227:117616.
13. Zhang H, Schneider T, Wheeler-Kingshott CA, Alexander DC. NODDI: Practical in vivo neurite orientation dispersion and density imaging of the human brain. *NeuroImage*. 2012; 61:1000-1016.

How to cite this article: Rodríguez-Galván JR, París G, Tristán-Vega A, Alberola-López C. Diffusion sampling schemes: A generalized methodology with nongeometric criteria. *Magn Reson Med*. 2023;1-11. doi: 10.1002/mrm.29605